

Crystal structure and defects visualization of $\text{Cu}_2\text{ZnSnS}_4$ nanoparticles employing transmission electron microscopy and electron diffraction

Nessrin Kattan^a, Bo Hou^{b,1}, David J. Fermín^{b,*}, David Cherns^{c,*}

^a Bristol Centre for Functional Nanomaterials, Tyndall Avenue, Bristol BS8 1FD, UK

^b School of Chemistry, University of Bristol, Cantocks Close, Bristol BS8 1TS, UK

^c HH Wills Physics Laboratory, University of Bristol, Tyndall Avenue, Bristol BS8 1TL, UK

ARTICLE INFO

Article history:

Received 29 June 2015

Received in revised form 11 August 2015

Accepted 13 August 2015

Keywords:

$\text{Cu}_2\text{ZnSnS}_4$

Kesterite

Nanoparticles

Transmission electron microscopy

Defects

Electron diffraction

ABSTRACT

A detailed analysis of the structure of $\text{Cu}_2\text{ZnSnS}_4$ (CZTS) nanocrystals synthesized by hot-injection in the presence of oleylamine is provided employing high resolution TEM, selected area electron diffraction (SAED) and convergent beam electron diffraction (CBED). The nanostructures were investigated as-grown and after vacuum thermal treatment at 550 °C. As-grown materials consisted of polycrystalline particles with an average size of 7 ± 3 nm, which grow an average size of 53 ± 13 nm after the vacuum annealing step. This thermal treatment allows investigating the initial stages of high quality film growth required in photovoltaic devices. Sets of SAED and CBED patterns, where individual crystals after annealing were viewed down different prominent zone axes, enabled us to reveal the presence of weak reflections due to cation ordering, and confirm a tetragonal unit cell consistent with either the kesterite or stannite structure. We demonstrate how these approaches enable to distinguish CZTS from secondary phases such as ZnS. Structure defects of partially annealed CZTS crystals were also investigated using bright and dark field images taken in 2-beam diffraction conditions as well as by high resolution lattice imaging. The material exhibited dislocations, along with lamellar twins and stacking faults characterized by local hexagonal structure on $\{112\}$ planes. High resolution TEM images showed preferential growth on $\{112\}$ planes during vacuum annealing, which is consistent with X-ray diffraction patterns. These studies provide key information on nanoscale crystal defects which may have important consequence on the performance of CZTS photovoltaic devices.

© 2015 The Authors. Published by Elsevier Ltd. This is an open access article under the CC BY license (<http://creativecommons.org/licenses/by/4.0/>).

1. Introduction

$\text{Cu}_2\text{ZnSnS}_4$ (CZTS) is key material towards the development of scalable thin-film photovoltaic technology considering the abundance and low-cost of the constituent elements as well as its direct bandgap (~ 1.4 eV) and high optical absorption coefficient ($\sim 10^4$ cm⁻¹) [1,2]. Attention has been drawn towards solution processible methods, such as bulk inorganic and nanoparticle synthesis which have produced devices with efficiencies exceeding 9% [3,4]. Nanoparticle precursors, such as those obtained by hot-injection methods, exhibit the advantage of controlling parameters such as phase, composition and particle size distribution prior to the deposition of CZTS ink [5,6]. In principle, this approach does not

require reactive annealing steps such as those used for sputtering, electrodeposition and molecular precursor deposition techniques. However, crystal growth from 10 nm to several micrometres without compromising the structure and composition of the material is a highly complex process which is not clearly understood.

In theory, CZTS can form three types of tetragonal crystal structures: Kesterite (space group $I4$), Stannite (space group $I42m$) and primitive-mixed CuAu (PMCA) structure (space group $P42m$) as shown in Fig. 1a. Kesterite type CZTS is derived from Chalcopyrite type CuInS_2 (CIS) by substituting of In atoms with Zn and Sn while stannite and PMCA are derived from a CuAu-like structure. The only difference between kesterite and stannite, which are tetragonal with $c \sim 2a$ (Fig. 1b), is the distribution of Cu and Zn within the unit cell while Sn atoms occupy the same position in both structures. The PMCA structure has $c \sim a$ which can be considered as a combination of two kesterite and stannite unit cells (Fig. 1a). However, this structure has not been observed experimentally. Based on density functional theory calculations, the kesterite type structure is the more stable energy structure with an energy difference of only ~ 3 meV/atom between stannite and kesterite [7].

* Corresponding authors.

E-mail addresses: David.Fermin@bristol.ac.uk (D.J. Fermín), D.Cherns@bristol.ac.uk (D. Cherns).

¹ Current address: Department of Engineering Science, University of Oxford, Parks Road, Oxford OX1 3PJ, UK.

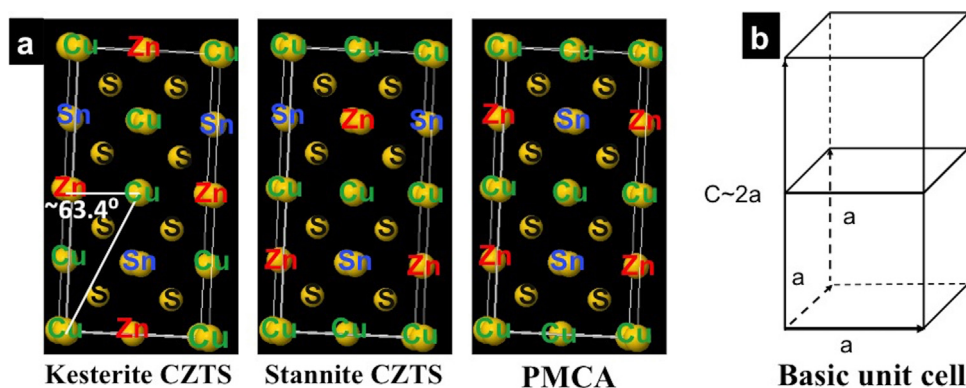


Fig. 1. (a) Tetragonal unit cells of kesterite, stannite and primitive-mixed CuAu (PMCA) of $\text{Cu}_2\text{ZnSnS}_4$. (b) A diagram of the tetragonal unit cell. All three unit cells are tetragonal, with the c -axis arrowed. For kesterite and stannite, $c \sim 2a$, whereas for PMCA, $c \sim a$ with two unit cells displayed to emphasize the difference in cation ordering between all three structures. The angle of 63.4° is a characteristic of a tetragonal unit cell and it will be used as an identification key for the kesterite/stannite structure. It should be mentioned that the value of this angle may slightly vary in off-stoichiometric CZTS, due to changes in the $c/2a$ ratio.

Distinguishing between these two structures is difficult due to the similarities in number of electrons (28 electrons) of Cu^+ and Zn^{2+} which result in closely similar X-ray and electron scattering factors while PMCA is distinguishable structure [8,9].

In addition to different structures of CZTS, secondary phases such as ZnS , Cu_2S , and Cu_2SnS_3 (CTS) are also likely to occur in the films as CZTS is thermodynamically stable in a narrow region from the phase diagram and the existence of these phases can greatly influence the performance of the device due to differences in the band alignment or a mismatch in the crystal structure [10–12]. Key secondary phases such as ZnS and CTS cannot easily be identified by conventional X-ray diffraction (XRD) given their highly similar patterns. The presence of crystallographic defects is also an important issue affecting the carrier transport and lifetime in the absorber layer. For example, efficient CdTe and CIGS devices exhibit minority carrier lifetime 1–2 orders of a magnitude longer than state-of-the-art CZTS [9,13]. The short carrier lifetime in CZTS has been linked to point defects, twinning, dislocations, stacking faults and Cu/Zn disordering [14,15].

In the present paper, we will provide an unprecedented structural analysis of CZTS nanoparticles synthesized by hot-injection based on high resolution electron microscopy (TEM), selected area electron diffraction (SAED) and convergent beam electron diffraction (CBED) techniques. As-grown and vacuum annealed particles will be investigated focusing on crystal orientation and the presence of secondary phases (ZnS). We provide a clear framework for identifying these materials analyzing characteristic electron diffraction “fingerprints”. We also use bright field (BF) and dark field (DF) TEM imaging to examine defects in CZTS nanocrystal after thermal annealing. We identify twinning and local hexagonal structures formed in the early stages of the film growth from nanoparticle precursors.

2. Materials and methods

Stoichiometric CZTS nanoparticles were synthesized following the procedures described previously [6,11]. Briefly, 1.5 mmol of copper (II) acetylacetonate, 0.75 mmol of zinc acetylacetonate hydrate, 0.75 mmol of tin (IV) bis(acetylacetonate) dichloride were added into 10 ml of oleylamine. A 3 ml of 1 M sulfur solution in oleylamine is injected into the previous solution at 225°C under inert condition and left for 30 min. The mixture was then cooled to $\sim 80^\circ\text{C}$ and washed by centrifugation using a mixture of toluene and isopropanol to precipitate the material and then the residue was collected and dried. The dried powder was annealed in a 3 cm vacuum sealed quartz tube at 550°C for 2 h. The as-grown and

annealed material was analyzed using TEM (Philips EM430 and JEOL 2010 microscopes) and X-ray diffraction performed using (BRUKER-AXS D8, $\text{Cu K}\alpha$ radiation $\lambda = 1.54 \text{ \AA}$).

3. Results and discussion

3.1. Thermogravimetric (TGA) and XRD analysis

Fig. 2a shows a characteristic thermogravimetric analysis (TGA) curve of as-grown CZTS nanoparticles. TGA was performed under N_2 atmosphere, showing a 10% weight loss below 100°C associated with the loss of moisture and solvents such as toluene and isopropanol. Between 100 and 400°C , approximately 20 wt% loss is observed which is linked to the removal of oleylamine adsorbed at the particle surface. This is consistent with the boiling temperature of oleylamine ($\sim 360^\circ\text{C}$). Mass loss stabilizes between 500 and 800°C . Based on these results, a temperature of 550°C was selected for thermal annealing under vacuum in a sealed quartz ampule as shown in Fig. 2b. Under this condition, we anticipate that SnS losses will be minimal and most of the products of the stabilizer desorption will re-deposit on the walls of the ampoules.

X-ray diffraction (XRD) patterns for as-grown and annealed CZTS are contrasted in Fig. 3. The as-grown material shows three broad peaks, which can be correlated with the three main peaks in the powder diffraction file of bulk kesterite CZTS (JCPDS 26-0575, $a = 5.435 \text{ \AA}$, $c = 10.869 \text{ \AA}$), 112, 220 and 312. These reflections could also be indexed as 111, 220 and 311 on a smaller tetragonal (near cubic) cell where c has been halved. Weaker reflections henceforth referred to as superlattice reflections, which reveal the cation ordering, are not readily visible in the X-ray diffraction pattern.

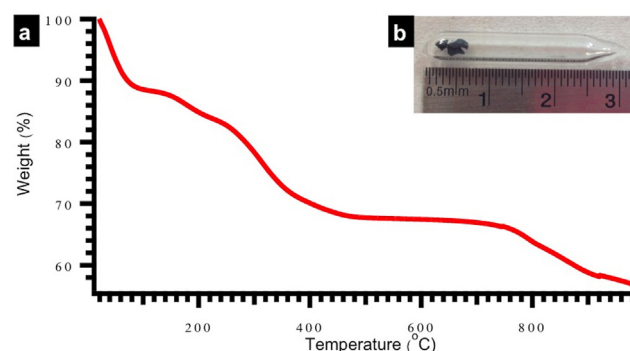


Fig. 2. (a) Thermogravimetric analysis of CZTS under N_2 atmosphere. (b) Picture of a quartz ampule for annealing CZTS as-grown particles under vacuum at 550°C .

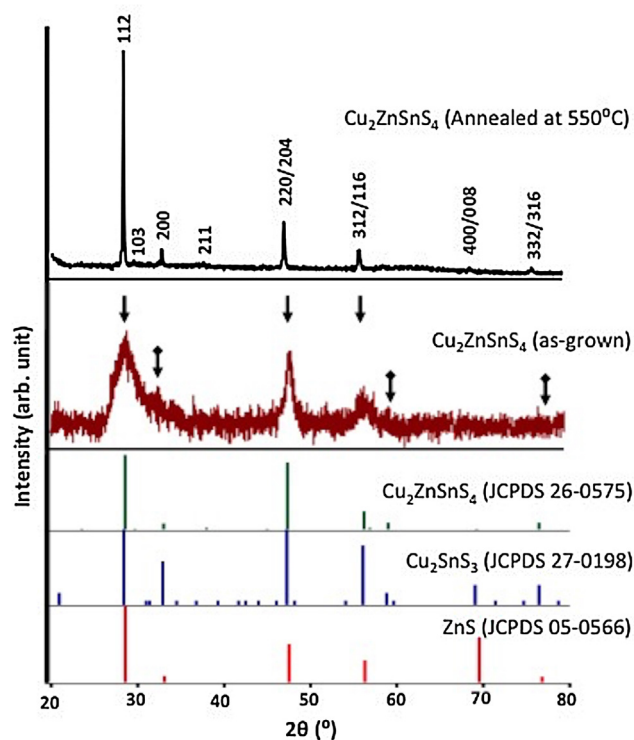


Fig. 3. Powder-XRD patterns of as-grown and after annealing CZTS. The patterns are consistent with the powder diffraction patterns of kesterite CZTS (JCPDS 26-0575), Cu_2SnS_3 (JCPDS 27-0198), and ZnS (JCPDS 05-0566).

For the as-grown sample, the average crystallite size has been estimated to be 7 ± 3 nm using the Scherrer equation under the assumption of spherical nanoparticles. The XRD pattern of the annealed material shows higher signal-to-noise ratio with sharper peaks in comparison to the as-grown material, suggesting an

increase in particle size. There are peaks at total diffraction angles 2θ of 28.4° at 112, 32.9° at 200, 47.3° at 220/204, 56.1° at 312/116, 69.1° at 400/008, and 76.4° at 332/316 reflection, where the indexing is again done on the basis of the kesterite/stannite unit cell. As for the as-grown sample, all these reflections could be understood on the basis of a near-cubic unit cell. There are weak features located at 29.6 and 37.9° which could be associated with superlattice reflections from the 103 and 211 planes. Although the XRD appears consistent with kesterite, this technique is rather insensitive to the specific cation ordering associated with kesterite, stannite and PMCA structures. In principle, the tetragonal unit cell of the stannite structure is slightly distorted from the kesterite unit cell due to the different arrangement of cations. This leads to small differences in diffraction angle (approximately 0.2°) for the high order peaks such as 220/204 and 116/312 between kesterite and stannite [11]. However, these differences cannot be reliably resolved with the average peak widths obtained for the nanostructures.

It should also be mentioned that there is very little difference in XRD patterns of CZTS between the phases in Fig. 1 and key secondary phases such as Cu_2SnS_3 and ZnS, as illustrated in Fig. 3. Therefore, the XRD is not a sufficient technique to reliably distinguish between these different phases. However, using SAED and CBED techniques in TEM allow us to clearly identify the tetragonal phases from cubic phases as illustrated in the following section. Another feature in Fig. 3 is the comparable peak intensity ratio for 112 and 220 in the as-grown material and the standard CZTS pdf file. However, the vacuum annealed material exhibits a significantly stronger 112 reflection which could be rationalized in terms of a pronounced (112) texture. This point will be confirmed by high-resolution TEM images below.

3.2. TEM and electron diffraction studies of CZTS nanoparticles

TEM images of as-grown CZTS are illustrated in Fig. 4a and d. It can be clearly seen that there is a dispersion in particle size, in which

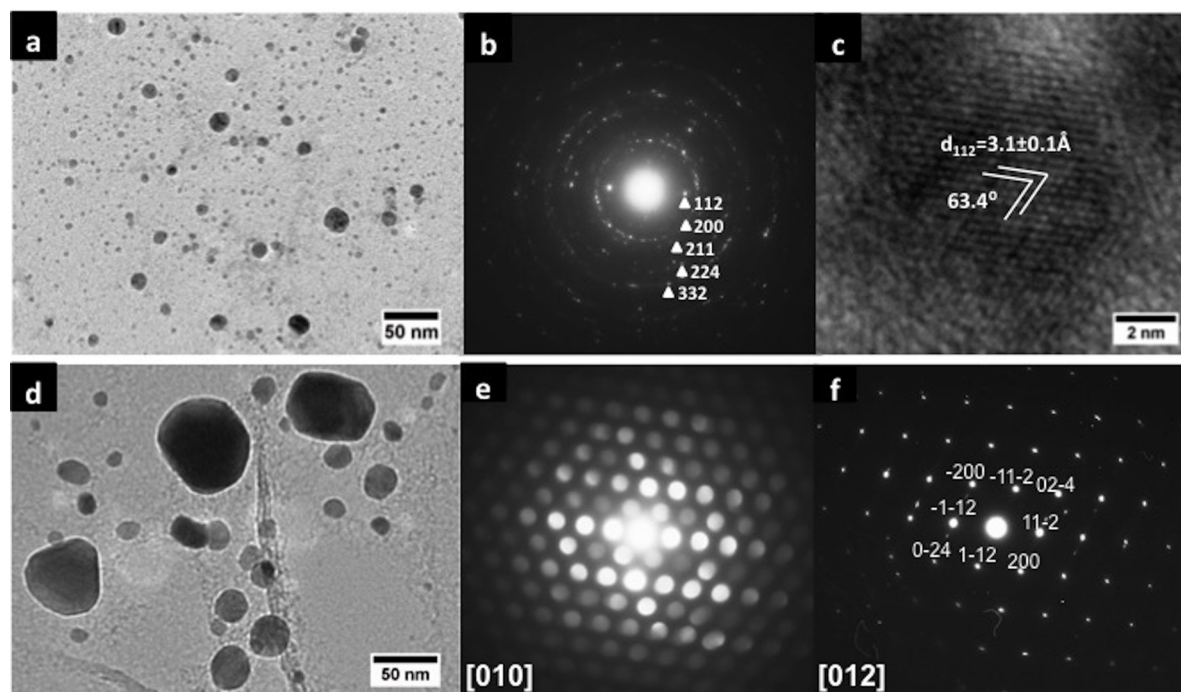


Fig. 4. (a and d) TEM images of as-grown nanoparticles illustrating their polydispersity. (b) SAED obtained for the smaller population of CZTS nanoparticles. (c) High resolution TEM of a 6 nm nanoparticle featuring d-spacing for the 112 plane and cross-grating patterns consistent with the superlattice kesterite structure. (e) and (f) illustrate the CBED and SAED of the larger nanostructures, respectively. The electron diffraction patterns were obtained at 200 kV and at a camera length of 267 mm.

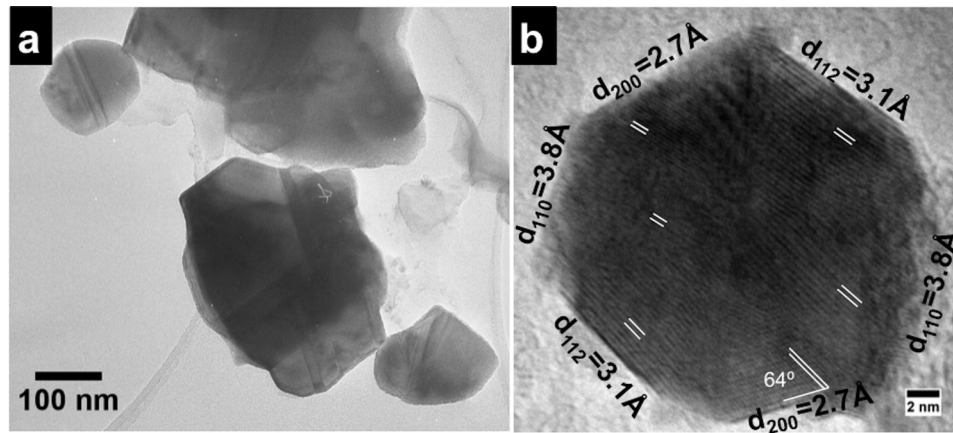


Fig. 5. (a) TEM and (b) high resolution TEM image of vacuum annealed CZTS nanocrystals.

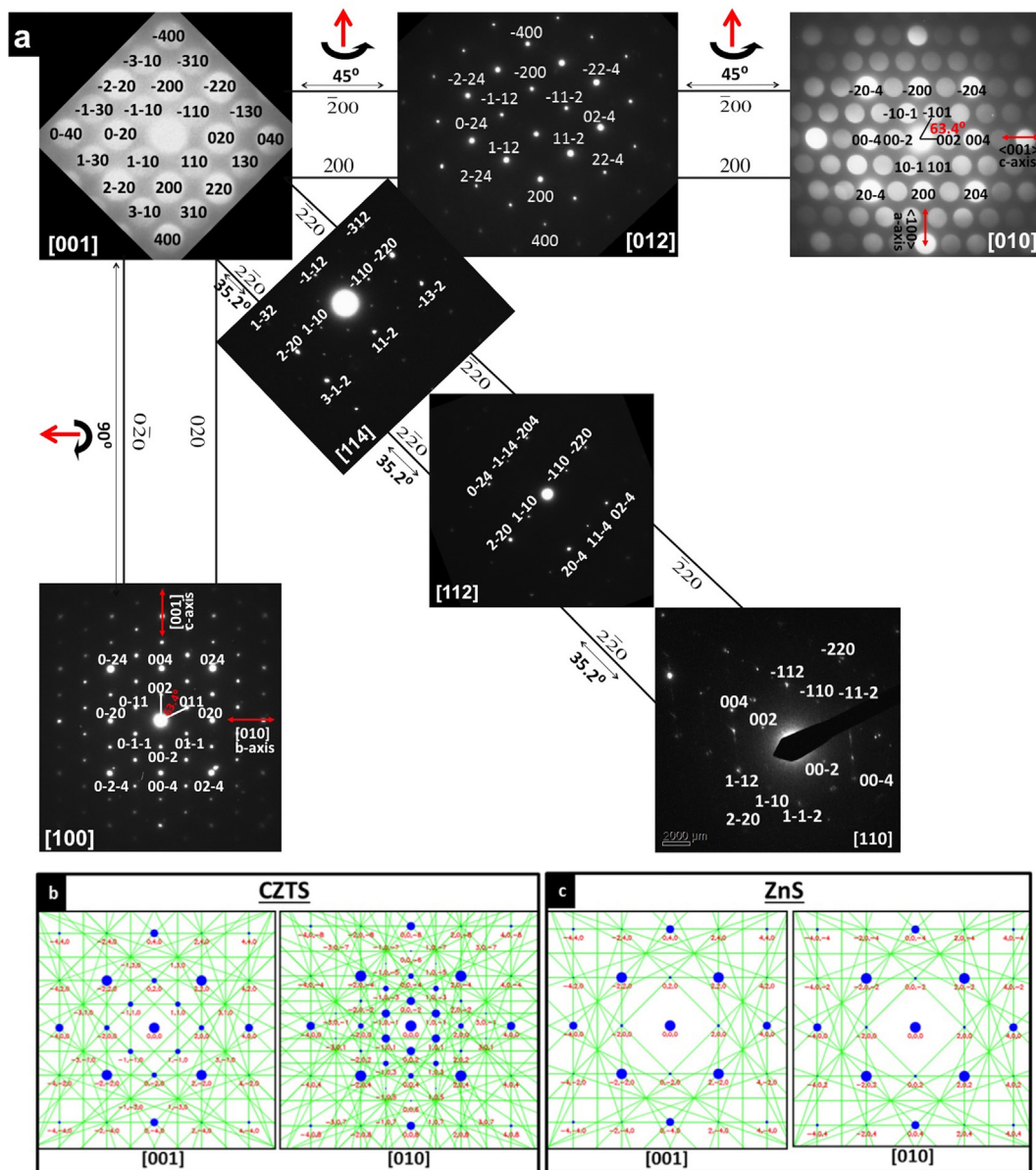


Fig. 6. (a) CBED and SAED patterns of vacuum annealed CZTS obtained by rotating a single nanocrystal based on the Kikuchi bands. Simulations of SAED patterns for the [001] and [010] zone axes of (b) CZTS and (c) ZnS. The diffraction patterns represent the fingerprints differentiating the tetragonal CZTS from the cubic ZnS phase.

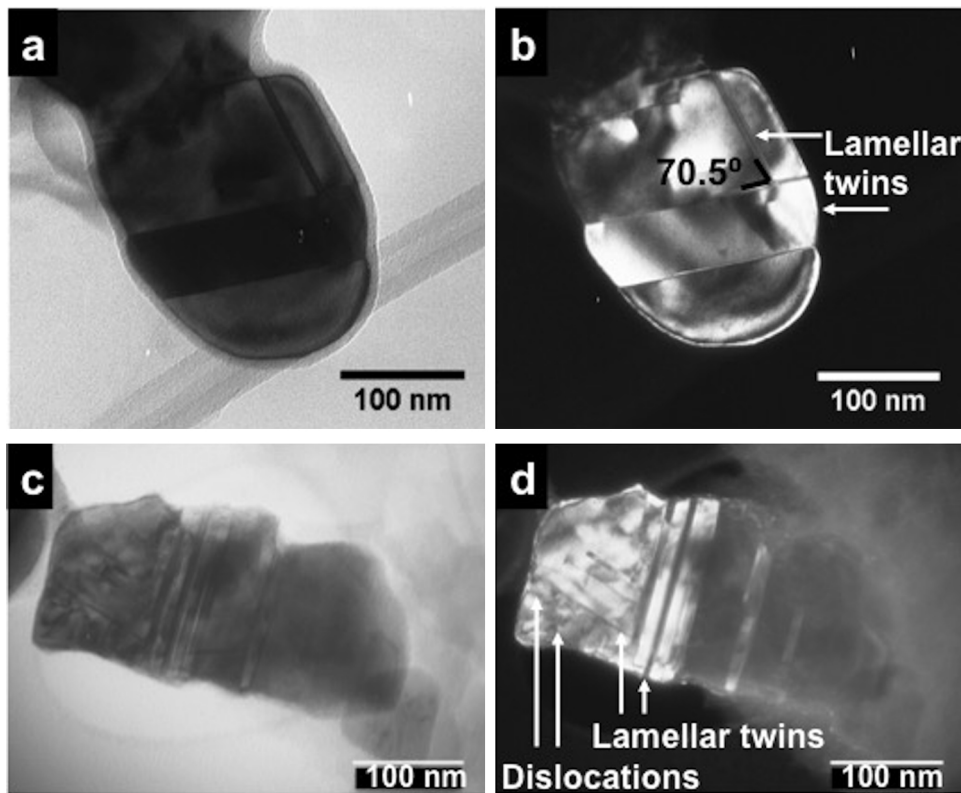


Fig. 7. TEM-bright field (a and c) and dark field (b and d) images of vacuum annealed CZTS nanoparticles featuring lamellar twin and dislocations.

the largest grains exhibit a mean diameter of 10 ± 2 nm. This particle size is close to the crystalline domain size obtained from the XRD peak broadening (Fig. 3). The SAED pattern in Fig. 4b exhibits polycrystalline diffraction rings consistent with 112, 200, 211, 224, and 332 kesterite reflections. The 211 ring can be taken as an evidence of the larger tetragonal unit cell expected for kesterite and stannite materials, but not for PMCA. Fig. 4c exhibits a high resolution TEM image featuring lattice fringes associated with a d-spacing of 3.1 ± 0.1 Å, consistent with 112 planes. Better defined CBED (Fig. 4e) and SAED patterns (Fig. 4f) can be obtained for the larger set of nanoparticles displayed in Fig. 4d. The hexagon of diffraction discs closest to the central disc in the [010] CBED pattern in Fig. 4e are evidence of the weak superlattice reflections related to the tetragonal unit cell. The ensemble of the data show that the structure of the small and large set of nanoparticles is consistent with the tetragonal structure linked to kesterite/stannite.

Thermal annealing in the vacuum ampule resulted in larger CZTS nanoparticles as displayed in Fig. 5a. The high resolution image in Fig. 5b is characterized by lattice fringes with d-spacing of 3.8, 3.1 and 2.7 nm associated with the {110}, {112} and {200} planes. The lattice spacing values are consistent with the XRD results and the expected kesterite/stannite structure. Figs. 4c and 5b also highlight

the 63.4° cross-grating angle associated with the tetragonal unit cell (Fig. 1).

Fig. 6 illustrates a selection of SAED and CBED patterns taken at different crystal zone axes from individual particles. The patterns were obtained by rotating the crystal using the Kikuchi bands which corresponded to diffraction from low index crystal planes. The [001] zone axis pattern views the unit cell along the tetragonal c-axis and exhibits four fold symmetry while the perpendicular [010] zone axis pattern has twofold symmetry due to the longer c-axis now being in the diffraction plane. The [010] zone axis pattern shows the angle of 63.4° indicated in the schematic diagram of the unit cell in Fig. 1 and also observed in diffraction patterns in Fig. 6a and in lattice images in Figs. 4c and 5b. The superlattice reflections are labelled in Fig. 6, including the 002, 101 and 110 reflections of the tetragonal unit cell.

Fig. 6b and c shows simulations of the diffraction patterns for kesterite CZTS and ZnS across the [001] and [010] zone axes [16]. Direct comparison with the experimental SAED patterns in Fig. 6a clearly shows that the annealed CZTS crystals have a tetragonal unit cell consistent with kesterite structure. The superlattice reflections in the SAED patterns are particularly distinctive in comparison to ZnS, providing a fingerprint for detecting this secondary phase.

Table 1

Lattice parameters of as-grown and annealed CZTS obtained by XRD, TEM and electron diffraction patterns.

CZTS	Technique	a (Å)	c (Å)	d ₁₁₂ -Spacing (Å)	Average particle size (nm)
As-grown	XRD	5.4 ± 0.2	10.8 ± 0.4	3.11	7 ± 3
	Diffraction patterns	5.39 ± 0.1	10.78 ± 0.1	3.08	–
	HR-TEM	5.32 ± 0.1	10.64 ± 0.1	3.07 ± 0.10	10 ± 5
Annealed	XRD	5.43 ± 0.01	10.87 ± 0.01	3.14	53 ± 13
	Diffraction patterns	5.35 ± 0.01	10.70 ± 0.02	3.08 ± 0.01	–
	HR-TEM	5.45 ± 0.1	10.90 ± 0.2	3.15 ± 0.10	–
Theoretical value (CZTS:JCPDS 26-0575)	XRD	5.427	10.848	3.126	–

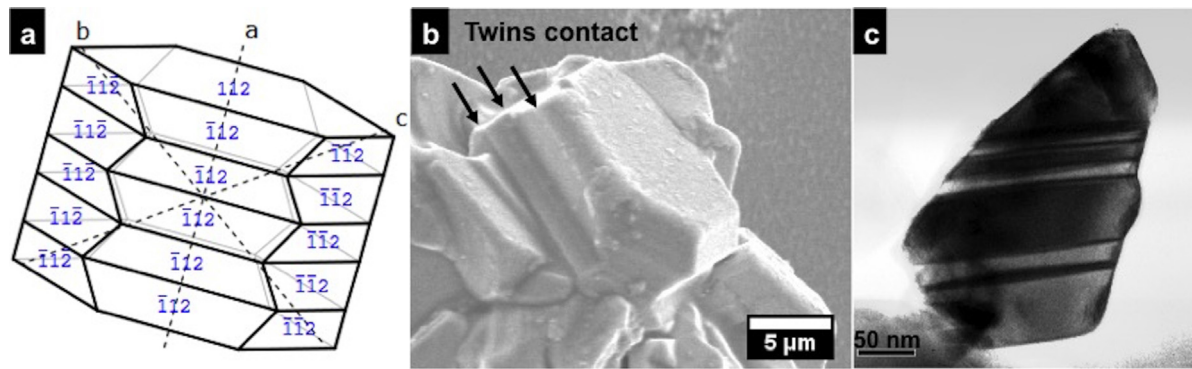


Fig. 8. (a) Schematic diagram of the preferential growth direction of CZTS crystals through $\{112\}$ lattice planes. SEM (b) and TEM (c) images of CZTS particles annealed at 1000 °C and 550 °C, respectively, illustrating the same crystal packing behaviour but at different length scales.

Moreover, identification of kesterite and stannite phases can be potentially achieved by comparing the relative intensities of the superlattice reflections such as 101 and 002, provided the film thickness is known. The uncertainty over the extent of ordering of Cu and Zn in the nanostructured materials prevents the identification of these phases at the present stage. We also expect the same analysis can be applied to Cu_2SnS_3 phases.

The structural parameters obtained from XRD, TEM and electron diffraction for the as-grown and vacuum annealed material are summarized in Table 1. The $c \sim 2a$ relationship defining the

tetragonal structure of these materials is confirmed by all techniques. It can be seen that not only a and c lattice constants but also the d_{112} spacing are consistent with the values extracted from the JCPDS 26-0575 standard.

3.3. Visualization of crystal defects in vacuum annealed CZTS nanoparticles

Fig. 7 contrasts bright field (BF) and dark field (DF) TEM images of vacuum annealed CZTS nanoparticles featuring a number of

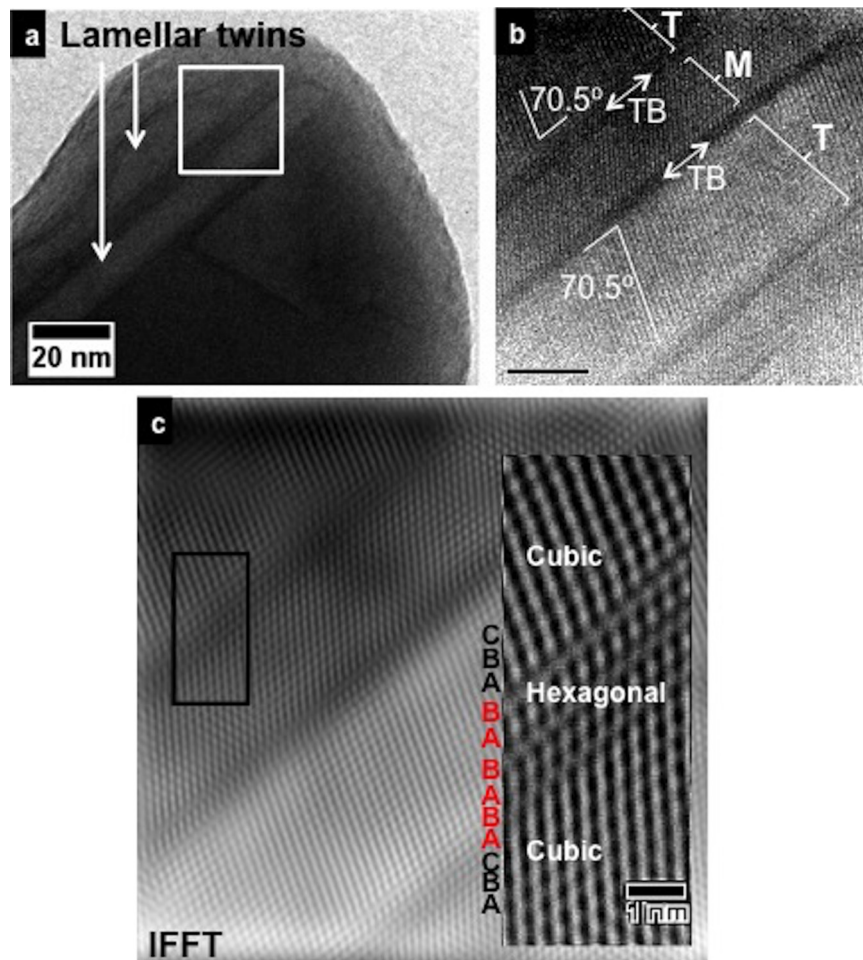


Fig. 9. (a) High resolution (TEM) images of the defects (lamellar twinning) in CZTS nanocrystals after annealing at 550 °C. (b) HRTEM lattice image of the twinning regions represented by the box in (a). (c) Inversed FFT analysis of the boundary regions of showing local hexagonal packing at twinning regions.

crystallographic defects. Both nanostructures were formed by growing lamellar twins on {112} planes. Fig. 7a and b show twinning on planes at relative angles of 70.5° . This is consistent with twinning on close-packed planes, corresponding to the {111} planes in cubic material, and the {112} planes in kesterite [9]. Similar structures can be observed in Fig. 7c and d, which also shows features associated with crystal dislocations. A thorough TEM analysis of the as-grown material did not provide any hint of these types of defects, strongly suggesting that these are generated as a result of the vacuum annealing process. This class of thermally promoted defects has been observed during the growth of other semiconductor materials and can be determined not only by the annealing temperature but also the cooling rate. Both stacking faults and dislocations can influence carrier transport properties, either through increased carrier scattering where the strain field varies (around dislocations), or due to small changes in the bandgap where the stacking changes locally from cubic to hexagonal. Density functional theory (DFT) calculations by Yan et al. confirmed that high density of stacking faults introduced a barrier to carrier migration in CIS and CdTe, and similar effects are expected in CZTS [14].

Fig. 8a schematically illustrates the preferential growth direction of CZTS nanocrystals based on electron microscopy observations which is also consistent with the strong 112 peak in the XRD pattern of annealed CZTS (see Fig. 2). Fig. 8b shows SEM images of CZTS particles annealed in nitrogen atmosphere at 1000°C , promoting extensive twinning contacting through {112} planes in the micron scale. The same behaviour is also observed after annealing at 550°C in vacuum but in the nanoscale as demonstrated in Fig. 8c. Fig. 8b and c show a comparison between the lamellar twins growth with particle size. This phenomenon can be rationalized in terms of the lower energy associated with the polar {112} with respect to the non-polar {220} surfaces [11], which have been reported not only for CZTS but also CIGS [17,18].

Examining at a higher resolution the structure generated by lamellar twinning reveals the formation of local hexagonal structures as illustrated in Fig. 9. The box in Fig. 9a shows the boundary between particles joined up after thermal annealing, featuring the characteristic 70.5° angle between adjacent planes as highlighted in Fig. 9b. Fig. 9b also shows deviation in the orientation of the close-packed planes on passing between the crystal matrix (M) and twinned regions (T). Inversed FFT analysis of the crystal boundary regions (Fig. 9c) highlights the local wurtzite structures present at the interface between the M and T regions. The plane stacking sequence at the interface can be represented as ABC-ABAB-ABC for the cubic-hexagonal-cubic boundaries. This local hexagonal structure will generate a localized electronic structure which can affect carrier transport across the film.

A key point to address at this stage is whether this type of defect further propagates in the transition from nanostructures to thin films. The vacuum annealing process employed in this work can be regarded as the initial stages in the formation of CZTS thin film from nanoscale precursors. Consequently, this class of defects could be ubiquitous to a variety of thin film preparation methods and understanding their impact on the electronic structure could reveal crucial information on the performance of this promising absorber material.

4. Conclusion

The structure of as-grown and partially annealed CZTS nanoparticles obtained by hot-injection was thoroughly examined by a

combination of X-ray, TEM and electron diffraction techniques. As grown nanoparticles with mean sizes of 10 ± 5 nm were characterized by broad XRD responses which provide an inconclusive determination of the phase purity of the material. However, electron diffraction patterns and images provide evidence of the superlattice structure characteristic of kesterite/stannite type CZTS. These features are significantly amplified upon annealing of the material in vacuum ampule, leading to an increase in the size of the particles to the range of ~ 100 nm. For the first time, we unveil the fingerprint for the tetragonal structure by CBED and SADP based. High resolution analysis of the annealed material clearly reveals preferential growth via stacking of {112} planes at different lengths scales. This is responsible for the high intensity of the 112 peak in the XRD. Furthermore, high-resolution TEM images confirm that particle growth during annealing leads to twinning and stacking faults on close-packed planes, which may act as barriers for carrier transport. In particular, we visualize the formation of local hexagonal phases in lamellar twin boundaries, which can play a role on carrier transport in thin absorber layers nucleated from nanoscale phase pure precursors.

Acknowledgments

The authors are grateful to Dr. Devendra Tiwari (School of Chemistry), Richard Webster (School of Physics) and Jonathan Jones (School of Chemistry) for their support to this work. The financial support by the EPSRC Centre for Doctoral the BCFN and the Taibah University (Saudi Arabia) is also acknowledges. DJF is also grateful to the EPSRC for funding through the PVTEAM programme (EP/L017792/1).

References

- [1] P. Jackson, D. Hariskos, E. Lotter, S. Paetel, R. Wuerz, R. Menner, W. Wischmann, M. Powalla, New world record efficiency for $\text{Cu}(\text{In}, \text{Ga})\text{Se}_2$ thin-film solar cells beyond 20%, *Prog. Photovolt.: Res. Appl.* 19 (7) (2011) 894–897.
- [2] K. Ito, T. Nakazawa, Electrical and optical properties of stannite-type quaternary semiconductor thin films, *Jpn. J. Appl. Phys.* 27 (11R) (1988) 2094.
- [3] W. Wang, M.T. Winkler, O. Gunawan, T. Gokmen, T.K. Todorov, Y. Zhu, D.B. Mitzi, Device characteristics of CZTSSe thin-film solar cells with 12.6% efficiency, *Adv. Energy Mater.* 4 (7) (2014).
- [4] C.K. Miskin, W.-C. Yang, C.J. Hages, N.J. Carter, C.S. Joglekar, E.A. Stach, R. Agrawal, 9.0% efficient $\text{Cu}_2\text{ZnSn}(\text{S}, \text{Se})_4$ solar cells from selenized nanoparticle inks, *Prog. Photovolt.: Res. Appl.* 23 (5) (2015) 654–659.
- [5] U. Ghorpade, M. Suryawanshi, S.W. Shin, K. Gurav, P. Patil, S. Pawar, C.W. Hong, J.H. Kim, S. Kolekar, Towards environmentally benign approaches for the synthesis of CZTSSe nanocrystals by a hot injection method: a status review, *Chem. Commun.* 50 (77) (2014) 11258–11273.
- [6] B. Hou, D. Benito-Alifonso, N. Kattan, D. Cherns, M.C. Galan, D.J. Fermín, Initial stages in the formation of $\text{Cu}_2\text{ZnSn}(\text{S}, \text{Se})_4$ nanoparticles, *Chem. Eur. J.* 19 (47) (2013) 15847–15851.
- [7] S. Chen, X.G. Gong, A. Walsh, S.-H. Wei, Defect physics of the kesterite thin-film solar cell absorber $\text{Cu}_2\text{ZnSnS}_4$, *Appl. Phys. Lett.* 96 (2) (2010) 021902.
- [8] S. Schorr, Structural aspects of adamantine like multinary chalcogenides, *Thin Solid Films* 515 (15) (2007) 5985–5991.
- [9] B.G. Mendis, M.D. Shannon, M.C.J. Goodman, J.D. Major, R. Claridge, D.P. Halliday, K. Durose, Direct observation of Cu, Zn cation disorder in $\text{Cu}_2\text{ZnSnS}_4$ solar cell absorber material using aberration corrected scanning transmission electron microscopy, *Prog. Photovolt.: Res. Appl.* 22 (1) (2014) 24–34.
- [10] A. Walsh, S. Chen, S.-H. Wei, X.-G. Gong, Kesterite thin-film solar cells: advances in materials modelling of $\text{Cu}_2\text{ZnSnS}_4$, *Adv. Energy Mater.* 2 (4) (2012) 400–409.
- [11] Q. Guo, G.M. Ford, W.-C. Yang, B.C. Walker, E.A. Stach, H.W. Hillhouse, R. Agrawal, Fabrication of 7.2% efficient CZTSSe solar cells using CZTS nanocrystals, *J. Am. Chem. Soc.* 132 (49) (2010) 17384–17386.
- [12] T. Gershon, T. Gokmen, O. Gunawan, R. Haight, S. Guha, B. Shin, Understanding the relationship between $\text{Cu}_2\text{ZnSn}(\text{S}, \text{Se})_4$ material properties and device performance, *MRS Commun.* 4 (04) (2014) 159–170.

- [13] O. Gunawan, T.K. Todorov, D.B. Mitzi, Loss mechanisms in hydrazine-processed $\text{Cu}_2\text{ZnSn}(\text{Se}, \text{S})_4$ solar cells, *App. Phys. Lett.* 97 (23) (2010) 233506.
- [14] Y. Yan, K.M. Jones, C.S. Jiang, X.Z. Wu, R. Noufi, M.M. Al-Jassim, Understanding the defect physics in polycrystalline photovoltaic materials, *Phys. B: Cond. Matter* 401 (2007) 25–32.
- [15] M. Grossberg, J. Krustok, T. Raadik, M. Kauk-Kuusik, J. Raudoja, Photoluminescence study of disordering in the cation sublattice of $\text{Cu}_2\text{ZnSnS}_4$, *Curr. Appl. Phys.* 14 (11) (2014) 1424–1427.
- [16] J.M. Zuo, J.C. Mabon, Web-based electron microscopy application software, Web-EMAPS, *Microsc. Microanal.* 10 (Suppl 2) (2004) <http://emaps.mrl.uiuc.edu/> (accessed 18.05.15).
- [17] D. Liao, A. Rockett, Epitaxial growth of $\text{Cu}(\text{In}, \text{Ga})\text{Se}_2$ on $\text{GaAs}(110)$, *J. App. Phys.* 91 (4) (2002) 1978–1983.
- [18] F. Liu, Y. Li, K. Zhang, B. Wang, C. Yan, Y. Lai, Z. Zhang, J. Li, Y. Liu, In situ growth of $\text{Cu}_2\text{ZnSnS}_4$ thin films by reactive magnetron co-sputtering, *Sol. Energy Mater. Sol. Cells* 94 (12) (2010) 2431–2434.